

Numerical simulation of round robin numerical test on tunnels using a simplified kinematic hardening model

Grigorios Tsinidis · Kyriazis Pitilakis ·
Areti Despina Trikalioti

Received: 29 March 2013 / Accepted: 18 November 2013 / Published online: 14 December 2013
© Springer-Verlag Berlin Heidelberg 2013

Abstract The paper summarizes the numerical simulation of the round robin numerical test on tunnels performed in Aristotle University of Thessaloniki. The main issues of the numerical simulation are presented along with representative comparisons of the computed response with the recorded data. For the simulation, the finite element method is implemented, using ABAQUS. The analyses are performed on prototype-scale models under plane strain conditions. While the tunnel behavior is assumed to be elastic, the soil nonlinear behavior during shaking is modeled using a simplified kinematic hardening model combined with a von Mises failure criterion and an associated plastic flow rule. The model parameters are adequately calibrated using available laboratory test results for the specific fraction of sand. The soil–tunnel interface is also accounted and simulated adequately. The effect of the interface friction on the tunnel response is investigated for one test case, as this parameter seems to affect significantly the tunnel lining axial forces. Finally, the internal forces of the tunnel lining are also evaluated with available closed-form solutions, usually used in the preliminary stages of design and compared with the experimental data and the numerical predictions. The numerical analyses can generally reproduce reasonably well the recorded response. Any differences between the experimental data and the numerical results are mainly attributed to the simplification

of the used model and to differences between the assumed and the actual mechanical properties of the soil and the tunnel during the test.

Keywords Centrifuge tests · Circular tunnels · Dynamic analysis · RRTT

1 Introduction

Underground structures and tunnels are nowadays frequently constructed to facilitate different needs (e.g., subways, underground parking stations, storage units, sewages, etc.), especially in densely populated areas. Considering their significance for life safe and economy, their proper seismic design is of great importance, especially in seismic-prone areas.

In general, during past earthquakes, tunnels were found to be less vulnerable than aboveground structures. However, several cases of extensive damage or even collapse are reported in the literature. The collapse of the under construction (up to that date) twin Bolu tunnels, during the 1999 Kocaeli earthquake, is an indicative example of bad performance [8, 12]. Generally, moderate-to-heavy damages were observed for peak ground accelerations (PGA) larger than 0.5 g, whereas for PGA smaller than 0.2 g, none to slight damages were reported. The lining type and the soil–lining interface conditions are of prior importance for the seismic behavior of a tunnel. Unlined tunnels or tunnels constructed with masonry found to be more vulnerable.

Embedded structures have geometrical and conceptual features that make their seismic behavior very distinct from surface structures [8, 11, 26]. The ground deformations, introduced by the surrounding soils, are prevailing, while

G. Tsinidis (✉) · K. Pitilakis · A. D. Trikalioti
Research Unit: Soil Dynamics and Geotechnical Earthquake
Engineering, Department of Civil Engineering, Aristotle
University of Thessaloniki, Thessaloniki, Greece
e-mail: gtsinidi@civil.auth.gr

K. Pitilakis
e-mail: kpitilak@civil.auth.gr
URL: <http://users.auth.gr/kpitilak/>

the inertial forces are of secondary importance. Generally, during an earthquake, tunnels can be affected by ground shaking and/or permanent displacements caused by ground failure (i.e., liquefaction, slope instabilities, fault displacements). During ground shaking, the tunnel can be deformed in various modes, both in the longitudinal and transverse directions, e.g., longitudinal axial deformation, longitudinal bending, cross-sectional compression, and cross-sectional ovaling [17]. The latter is of prior importance, as it can cause large stresses on the tunnel's lining.

Several methods have been proposed in the literature for the seismic design, based on different levels of complexity, ranging from closed-form solutions (e.g., to compute the lining internal forces) and simplified uncoupled methods, to the more accurate full dynamic time-history analysis of the soil–tunnel system [6, 8, 10, 18, 26]. A comprehensive review was made by Pitilakis and Tsinidis [19]. The results of these methods may significantly deviate, even under the same assumptions, demonstrating the relative lack of knowledge regarding the seismic behavior and design of tunnels. Several crucial parameters, such as the proper estimation of the design input motion, the distribution and the magnitude of the seismic shear stresses around the tunnel, and adequate for tunnels impedance functions, are among the open issues that need further research.

To this end, dynamic centrifuge tests were carried out on a circular tunnel model embedded in dry sand. The tests were performed in 2007 at the geotechnical centrifuge facility of the University of Cambridge (Schofield Centre), by researchers of University of Napoli Federico II, within the framework of the ReLUIIS Project (2005–2009) [14, 15]. Experimental data of two of these tests were made available to the scientific community within the round robin numerical test on tunnels (RRTT) organization.

In this paper, we describe the numerical simulation of the tests, performed in Aristotle University of Thessaloniki. The numerical results are presented and compared with the experimental data, in terms of accelerations, soil surface settlements, soil shear strains, and dynamic internal forces of the tunnel lining. The tunnel response, in terms of internal forces of the lining, is also evaluated using available closed-form solutions [18, 26], usually used during preliminary stages of design of tunnels.

2 Dynamic centrifuge tests

A series of dynamic centrifuge tests was carried out on a circular aluminum model tunnel embedded in dry sand, under centrifuge accelerations of 80 and 40 g [14, 15]. The tests were performed, using a small laminar box (500 × 250 × 300 mm³), at the 10-m-diameter “Turner Beam Centrifuge” of the Schofield Centre of the

University of Cambridge. Earthquake input motions were applied using the Stored Angular Momentum (SAM) actuator, which is designed to apply sinusoidal input motions [16].

The soil models were made using dry Leighton Buzzard sand (fraction E) reconstituted at two different relative densities (about 40 and 75 %). The physical properties of the sand are summarized in Table 1. The circular tunnel model was manufactured by an aluminum tube having an external diameter $D = 75$ mm and a thickness $t = 0.5$ mm. The mechanical properties of the specific aluminum alloy are tabulated in Table 2. The burial depth of the tunnel, for the cases studied herein, was set equal to two times the diameter (deep test cases T3 and T4 according to Lanzano et al. [15]). Test T3 refers to the dense sand case, while Test T4 refers to the loose sand case.

The models were instrumented using miniature piezo-electric accelerometers to measure the horizontal and the vertical accelerations at several locations in the soil and on the laminar box. Moreover, the tunnel was instrumented with strain gauges to measure the bending moments and the axial forces of the lining at four locations along 2 transverse sections (at the mid-span of the tunnel model and 50 mm aside to check the plane strain conditions). Two linear variable differential transducers (LVDTs) were attached on two gantries running above the model to measure the soil surface settlements. The final model setup and the instrumentation scheme of the cases studied herein are presented in Fig. 1.

During testing, the models were swung up to 80 g in steps of 10 g, and then, the earthquakes (sine waves of increasing amplitude and frequency) were fired in a row, leaving some time between them to acquire the data. After four earthquakes, the centrifuge was slowed to 40 g and one or two more earthquakes were fired. The main characteristics of the input motions are tabulated in Table 3. More details regarding the testing procedure may be found in Lanzano et al. [15].

Table 1 Sand physical properties (after [15])

G_s	e_{\max}	e_{\min}	d_{50} (mm)	d_{10} (mm)	d_{60}/d_{10}
2.65	1.014	0.613	0.140	0.95	1.58

Table 2 Mechanical properties of the aluminum alloy (after [15])

Unit weight, γ (kN/m ³)	Elastic modulus, E (GPa)	Poisson ratio, ν	Tensile yield stress, f_{yk} (MPa)	Tensile strength, f_{bk} (MPa)
27	70	0.33	500	600

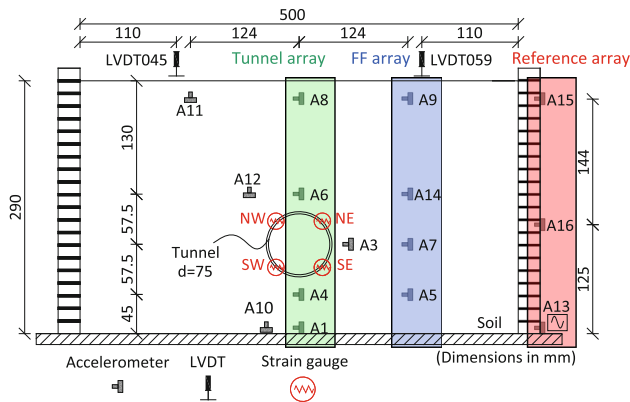


Fig. 1 Models layout, instrumentation scheme for T3 test case (A12 and A13 are reversed for T4), modified after [15]

Table 3 Earthquake input motions (bracketed values in prototype scale); after [15]

Input	Gravity level (g)	Frequency (Hz)	Duration (s)	Nominal amplitude (g)
EQ1	80	30 {0.375}	0.4 {32}	4.0 {0.05}
EQ2		40 {0.5}		8.0 {0.10}
EQ3		50 {0.625}		9.6 {0.12}
EQ4		60 {0.75}		12.0 {0.15}
EQ5	40	50 {1.25}	0.4 {16}	6.0 {0.15}
EQ6		40 {1.0}		5.0 {0.125}

3 Numerical analysis

3.1 Description of the numerical models

For the numerical simulation of the tests, we used the numerical code ABAQUS [1]. Full dynamic time-history analyses of the coupled soil–tunnel systems are performed, under plane strain conditions, on prototype-scale models (Fig. 2). Appropriate scaling laws are used to convert the computed quantities from prototype to model scale [20]. As the analyses are made in prototype scale, we examine only the earthquake cases that were fired under the same centrifuge acceleration (80 g), namely EQ1–EQ4 (according to Table 3). The analyses are performed assuming a linear elastic behavior for the tunnel-like specimen, while the soil behavior is modeled using a kinematic hardening model [2].

More specifically, the soil is meshed with 4-nodes quadratic plane strain elements, using a structured mesh technique, while the tunnel is modeled with beam elements. The adopted element size is selected in a way that ensures both (a) the efficient reproduction of all the waveforms of the whole frequency range under study and (b) the efficient simulation of the circular tunnel model. Therefore, a finer discretization near the tunnel model is

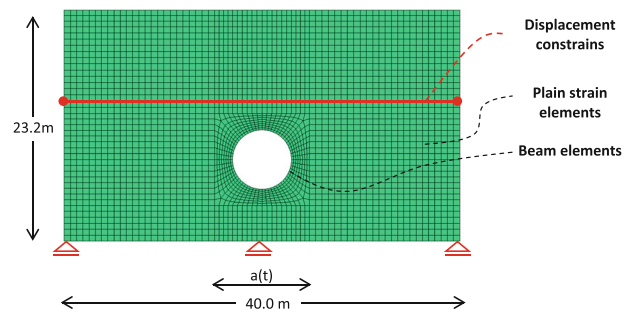


Fig. 2 Numerical model in ABAQUS

selected, allowing a low element aspect ratio (for the soil elements) and a low face corner angle (for the beam elements). A more refined model, used for preliminary sensitivity analysis and during the blind prediction analysis, had a negligible effect on the results [22], increasing significantly the computational cost.

The base boundary of the model is simulated as rigid bedrock, while for the vertical boundaries, kinematic constraints are introduced, forcing the opposite vertical sides to move simultaneously preventing any rotation, simulating in that simplified way the laminar box.

For the soil–tunnel interface, we use contact algorithms available in ABAQUS. The tangential behavior is modeled using the penalty friction formulation, assuming the full-slip conditions (Coulomb friction coefficient $\mu = 0$). Regarding the normal interface behavior, an exponential “softened” pressure–overclosure relationship is used. This method is selected because of its effectiveness to improve the computational cost without affecting the accuracy of the analysis. The model constrains the two media when attached, using the direct constraint enforcement method and Lagrange multipliers (when required), while it allows separation.

The effect of the interface tangential friction on the tunnel response is parametrically studied for the T3 test case. More specifically, except the full-slip conditions ($\mu = 0$), different values for the friction coefficient μ are used, namely 0.1 and 0.4. These coefficients correspond to soil–model interface friction angles equal to 5.7° and 21.8° , respectively. In a final analysis, the soil and the tunnel are fully bonded (no-slip conditions). As it will shown in the ensuing sections, this parameter that actually controls the shear stresses on the soil–tube interface is significantly affecting the lining axial forces.

Time discretization is an important element for the accuracy of the dynamic analysis. ABAQUS offers an automatic time incrementation scheme, according to which the time step of the analysis is properly selected and changed so as to achieve a stable solution. Due to the high nonlinearity of the problem studied herein, this scheme was

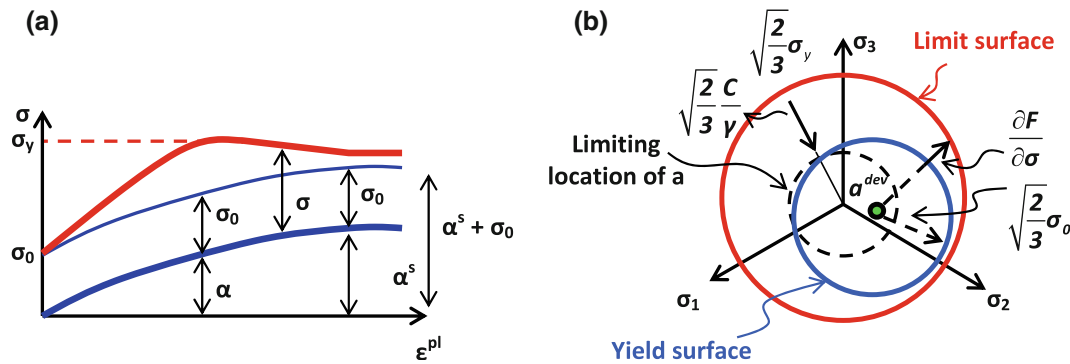


Fig. 3 Nonlinear isotropic/kinematic hardening constitutive soil model; **a** simplified one-dimensional and **b** three-dimensional representation of the hardening law (modified after [1] and [2])

selected as adequate to achieve convergence for the solution.

The input motion is introduced at the base boundary in terms of acceleration time histories, referring to the motion recorded at the reference accelerometer (Fig. 1). All the signals are filtered using a 4th-order Butterworth band-pass filter, for a wide range of frequencies (4–400 Hz) compared to the nominal frequency of each input motion.

For all the examined cases, the analyses are performed in two steps. In the first step, the gravity loads are introduced (e.g., geostatic step), while in the second step, the earthquake input motion is applied (dynamic implicit step).

3.2 Constitutive model

3.2.1 Constitutive relations

To model the soil nonlinear behavior during shaking, a kinematic hardening model combined with a von Mises failure criterion is used. The model, which is embedded in ABAQUS, may be considered appropriate for the cases where the behavior is normal pressure independent (e.g., clayey soils under undrained conditions). The version of the model used herein is appropriately modified, as described in detail by Anastasopoulos et al. [2], so as to account for the normal pressure and to be applicable for sandy, cohesion-less soils. To this end, the used model combines an extended pressure-depended von Mises failure criterion with a nonlinear kinematic hardening model and an associated plastic flow rule.

The general evolution of the stresses is described, as [1]:

$$\sigma = \sigma_o + \alpha \tag{1}$$

where σ_o corresponds to the zero plastic strain stress and α is the stress related with the kinematic evolution of the yield surface in the stress space (backstress). The yield surface is defined according to the following formulation:

$$F = f(\sigma - \alpha) - \sigma_o \tag{2}$$

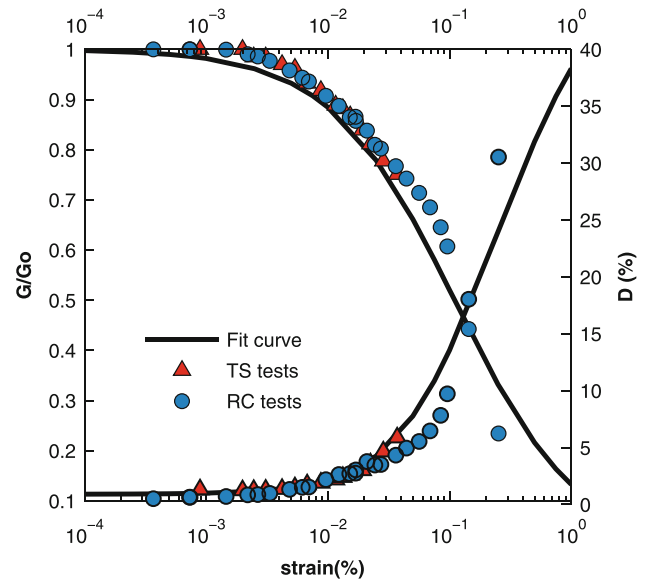


Fig. 4 G - γ - D curves adopted in the analyses (black solid line) versus triaxial shear (TS) and resonant column (RC) tests results (experimental laboratory results after [25])

where $f(\sigma - \alpha)$ is the equivalent Mises stress with respect to the backstress α .

The kinematic hardening model assumes associated plastic flow:

$$\dot{\epsilon}^{pl} = \dot{\epsilon}^{pl} \frac{\partial F}{\partial \sigma} \tag{3}$$

where $\dot{\epsilon}^{pl}$ is the rate of plastic flow and $\dot{\epsilon}^{pl}$ is the equivalent plastic strain rate.

The evolution law of the model comprises of an isotropic hardening component that describes the change of the equivalent stress, defining the size of the yield surface σ_o , as a function of plastic deformation and a nonlinear kinematic hardening component, which describes the translation of the yield surface in the stress space. The latter is defined as an additive combination of a kinematic

term and a relaxation term, which introduces the nonlinearity.

The isotropic hardening component actually describes the evolution of the yield surface size as a function of the equivalent plastic strain $\bar{\epsilon}^{pl}$, using the following simplified exponential law:

$$\sigma_o = \sigma_0 + Q_\infty \left(1 - e^{-b\bar{\epsilon}^{pl}}\right) \tag{4}$$

where σ_0 is the yield stress at zero plastic strain and Q_∞ and b are model parameters, defining the maximum change of the size of the yield surface and the rate of this change as plastic straining develops, respectively.

The evolution of the kinematic component of the yield stress is described according to the following formulation:

$$\dot{\alpha} = C \frac{1}{\sigma_o} (\sigma - \alpha) \dot{\bar{\epsilon}}^{pl} - \gamma \alpha \dot{\bar{\epsilon}}^{pl} \tag{5}$$

where C is the initial kinematic hardening modulus (equal to the elastic stiffness, as $C = \epsilon_y \sigma_y = E$) and γ a parameter that describes the rate at which the kinematic hardening decreases with the increasing plastic deformation.

The evolution of the two hardening components (isotropic and kinematic) is illustrated in Fig. 3 for unidirectional and multiaxial loading. The evolution law for the kinematic hardening component implies that the backstress α is contained within a cylinder of radius equal to $\sqrt{2/3}C/\gamma$. Since the yield surface remains bounded, any stress point must lie within a cylinder of a radius $\sqrt{2/3}\sigma_y$,

where σ_y is the maximum yield stress at saturation (large plastic strains).

In the case of cohesion-less soils (e.g., sands), the shear strength is controlled by the confining pressure and the friction angle φ . This pressure dependency is introduced in the model by defining the yield stress at saturation as a function of the octrahedral stress and the friction angle φ of the sand:

$$\sigma_y = \sqrt{3} \left(\frac{\sigma_1 + \sigma_2 + \sigma_3}{3} \right) \sin \varphi \tag{6}$$

where σ_1 , σ_2 , and σ_3 are the principles stresses. Since $\sigma_y = C/\gamma + \sigma_0$, γ can be computed, for cohesion-less soils, as follows:

$$\gamma = \frac{C}{\sqrt{3} \left(\frac{\sigma_1 + \sigma_2 + \sigma_3}{3} \right) \sin \varphi - \sigma_0} \tag{7}$$

Parameter σ_0 that controls the initiation of the nonlinear behavior (yield stress at zero plastic strain) is defined as a fraction λ of the yield stress σ_y (λ typically ranging from 0.1 to 0.3):

$$\sigma_0 = \lambda \sigma_y \tag{8}$$

Parameter C is actually the small-strain Young’s modulus, and it is computed for the cases studied herein, as described in detail, in the following. Generally, it is possible to express this parameter as a function of σ_y (not performed herein):

$$C = a \sigma_y \tag{9}$$

The modified kinematic hardening constitutive model is encoded in the ABAQUS environment through a user-defined subroutine [2].

The model can easily be implemented, as the required model parameters (λ , a) can be calibrated having only the following: (1) the soil strength (e.g., φ for sands), (2) the

Table 4 Parameters of the modified hyperbolic model for the G – γ – D curves

Parameter	γ_{ef}	n	a_1	a_2	a_3
Value	0.11	0.85	43.24	–92.15	49.79

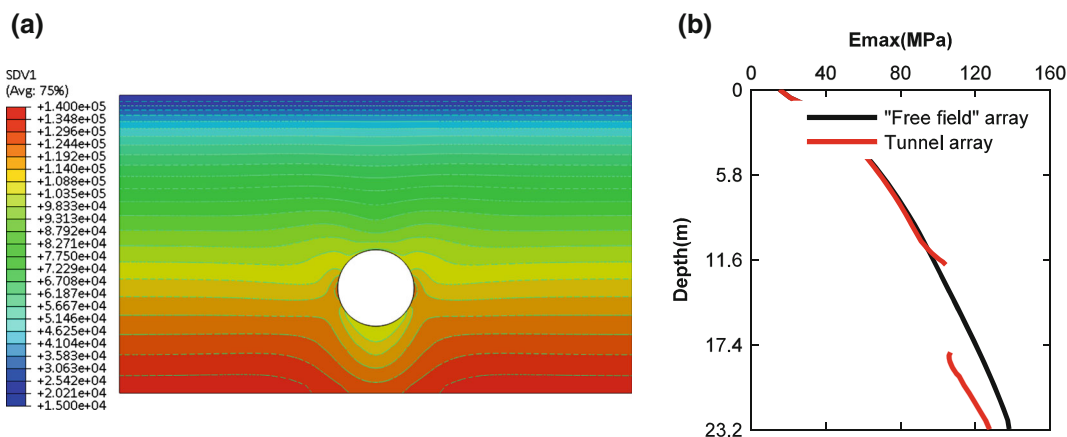


Fig. 5 Small-strain Young modulus for T3; **a** distribution around the tunnel, **b** distributions with depth along the tunnel, and the “free-field” array

Table 5 Soil mechanical properties adopted

Parameter	G_{max}	ρ (t/m ³)	Poisson ratio, ν	Rayleigh damping (%)	φ (°)	ψ (°)	c (MPa)	λ
Test T3								
Value	Hardin and Drenvich distribution, reduced	1.55	0.333	6	33.4	–	0.002	0.1
Test T4								
Value	Hardin and Drenvich distribution, reduced	1.43	0.333	6	33.4	–	0.002	0.1

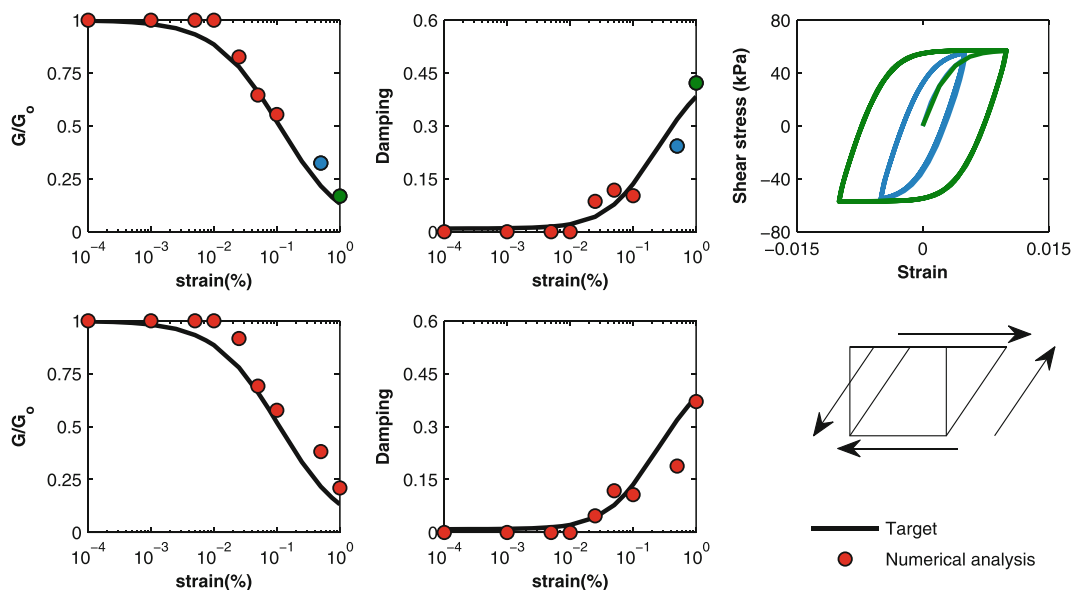


Fig. 6 Calibration of the constitutive model against the “target” $G-\gamma-D$ curves for a confining pressure of 100 kPa. *First line* results for T3 case, and *second line* results for T4 case. Shear stress–strain loops corresponding to the mentioned points (0.5, 1.0 %); T3 test case

small-strain elastic modulus, and (3) adequate $G-\gamma-D$ curves for the studied soil fraction. The selection of these parameters (only λ in this case) is presented in the following section along with the calibration procedure for the cases studied.

It is mentioned that the implemented model constitutes an approximation of the actual sand behavior. The model, despite its simplicity regarding the description of the volumetric strains, is found capable to reproduce several aspects of the recorded response, with reasonable engineering accuracy. Similar observations are made by Anastasopoulos et al. [2].

3.2.2 Model calibration

The $G-\gamma-D$ curves required for the model calibration are derived from laboratory tests results (resonant column and triaxial shear tests) for the specific sand fraction [25]. More specifically, a modified hyperbolic model was used to fit of the experimental results, where the G/G_{max} variation with the shear strain is expressed as [5]:

$$\frac{G}{G_{max}} = \frac{1}{1 + (\gamma/\gamma_{ef})^n} \tag{10}$$

where G_{max} is the small-strain shear modulus, G is the reduced shear modulus corresponding to the shear strain level γ , γ_{ef} is the reference strain (corresponding to the strain amplitude for $G/G_{max} = 0.5$), and n is the curvature coefficient. The curvature coefficient and the reference strain are the two fitting parameters of the model, with the prior expressing the overall slope of the $G/G_{max}-\log\gamma$ curve and the latter expressing the linearity of the $G/G_{max}-\log\gamma$ curve. The damping ratio $DT(\%)$ was then given a function of G/G_{max} according to the following expression:

$$DT(\%) = \alpha_1 \times \left(\frac{G}{G_o}\right)^2 + \alpha_2 \times \left(\frac{G}{G_o}\right) + \alpha_3 \tag{11}$$

Figure 4 portrays the adopted $G-\gamma-D$ curves in comparison with the laboratory test results, while Table 4 tabulates the fitting parameters values.

For the estimation of the sand small-strain shear modulus (“elastic” stiffness), a trial and error procedure was performed for each test case. More specifically, 1D

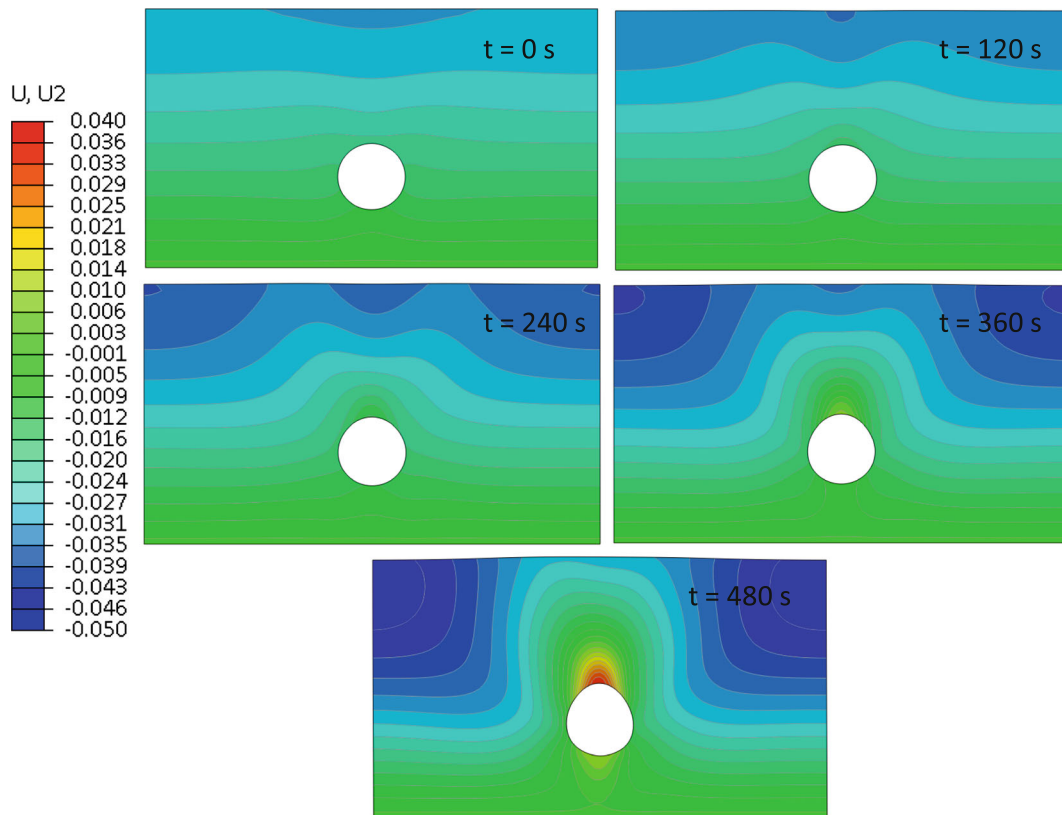


Fig. 7 Soil settlements computed for model T3 during several stages of the analysis, plotted on the deformed shape model (in prototype scale; scale factor $\times 15$)

equivalent linear soil response analyses of the soil deposits were performed, using the G – γ – D curves presented before and different distributions of the small-strain elastic modulus. The analyses were performed in the frequency domain using EERA [3]. The results of these analyses, in terms of horizontal acceleration at the free-field array, were compared with the recorded data. The finally adopted distribution of the small-strain elastic modulus was estimated so as to achieve the best fitting of the numerical predictions with the experimental results. This procedure revealed that a reduced distribution according to Hardin and Drnevich [7] was adequately reproducing the small-strain shear modulus. To this end, the following distribution was used for the description of the small-strain shear modulus:

$$G_{\max} = 0.35 \times 100 \frac{(3 - e)^2}{1 + e} (\sigma')^{0.5} \quad (12)$$

where e is the void ratio, σ' is the mean effective stress (in MPa), and G_{\max} is the shear modulus (in MPa). These reduced values for the soil shear modulus are in accordance with the results presented by Lanzano et al. [14], who computed the average shear modulus mobilized during each shake from experimentally derived top-to-base transfer functions.

In the final 2D dynamic analysis, small-strain shear modulus, G_{\max} , is introduced through a user subroutine. It is noted that as G_{\max} is correlated with the mean effective stress, its distribution around the vicinity area of the tunnel is affected by the presence of the tunnel (effect on the mean effective stress). Figure 5 presents the distribution of the small-strain elastic modulus as computed for T3 test with the aforementioned formulation; the distribution with depth along the tunnel array and along the “free field” array is also compared. The presence of the tunnel affects the distribution around the tunnel as expected.

Regarding the strength parameters for the soil, we adopted the laboratory test results for the specific fraction of sand [25], as presented in Table 5.

To implement the kinematic hardening model to the present study, model parameter (λ) was systematically calibrated for various levels of the overburden stress using the aforementioned G – γ – D curves and G_{\max} distribution. For this purpose, numerical simulation of cyclic simple shear tests was conducted. Figure 6 presents the comparisons between the “target” and the computed G – γ – D curves for a mean effective stress equal to 100 kPa. Representative shear stress–strain loops are also presented for two shear strain levels as computed during the calibration procedure of T3 test.

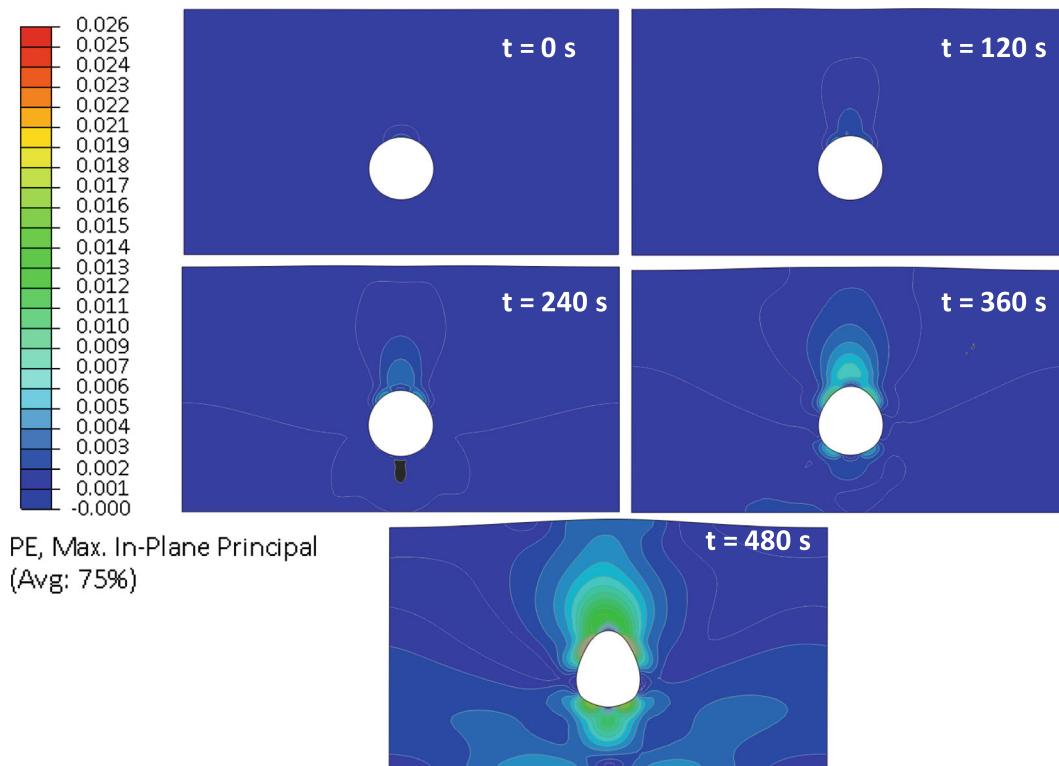


Fig. 8 Soil plastic deformation computed for model T4 during several stages of the analysis, plotted on the deformed shape model (scale factor $\times 15$)

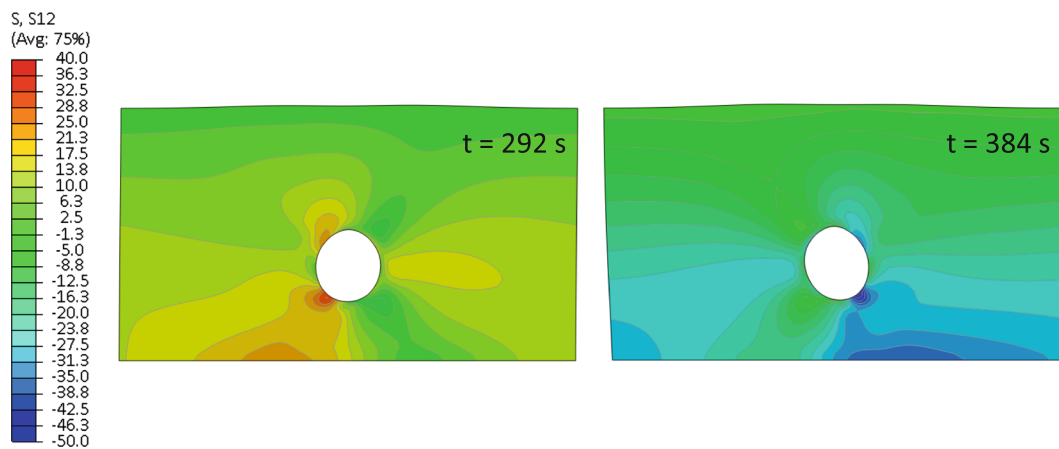


Fig. 9 Soil shear stresses around the tunnel during shaking in kPa (model T3; scale factor $\times 30$)

4 Numerical predictions versus experimental results

In this section, we present representative numerical results compared to the experimental data, in terms of accelerations, soil shear strains, soil surface settlements, and dynamic internal forces of the model lining. They are generally shown at model scale, if not differently stated.

4.1 Models deformed shapes

Figure 7 presents the soil settlements of model T3 computed in intermediate and the final stage of the analysis. Similar deformed shapes of model T4 are presented in Fig. 8 where, instead of the soil settlements, the computed soil plastic deformations are presented in contour diagrams.

The results indicate that in both tests, the soil settles slightly more at the free field (compared to the area above the tunnel), causing a small inward horizontal deformation of the tunnel. Representative deformed shapes of the soil–tunnel system during shaking (model T3) are presented in Fig. 9, where the soil shear stresses are plotted in contour diagrams.

4.2 Accelerations

Figures 10, 11, 12, and 13 present time windows of the computed and recorded acceleration time histories for different earthquake scenarios for both tests T3 and T4, while in Figs. 14 and 15, the maximum computed horizontal accelerations along vertical accelerometers arrays are compared to the experimental values for all the earthquakes studied. The numerical predictions are generally in good agreement with the records for the horizontal acceleration. The differences, generally minor, are mainly attributed to the differences between the assumed soil mechanical properties (stiffness and damping) and their actual values during the test.

Small values of vertical acceleration were also recorded at several locations close to the base and inside the soil deposit.

These values are probably amplified by a reduced parasitic yawing moment of the laminar box on the shaking table that is not modeled in the numerical analyses. For this reason, the reported differences between the computed vertical acceleration and the recorded data are significant (A10, A11, and A12 for test T3 and A10, A11, and A13 for test T4).

4.3 Soil surface settlements

Figure 16 presents the recorded and computed surface settlements for both the tests. The numerical analyses generally underestimate the soil settlements (both static and dynamic) with respect to the experimental data. The experimental results may be biased to some extent by the way the LVDTs are fixed to the gantries of the box and by the small bending of these gantries caused by the strong gravity forces. Besides this fact, the observed differences may be attributed to the constitutive relationship used here to describe the sand behavior under dynamic loading.

4.4 Soil shear strains

The numerically computed soil shear strains are compared with the shear strains estimated, along the vertical

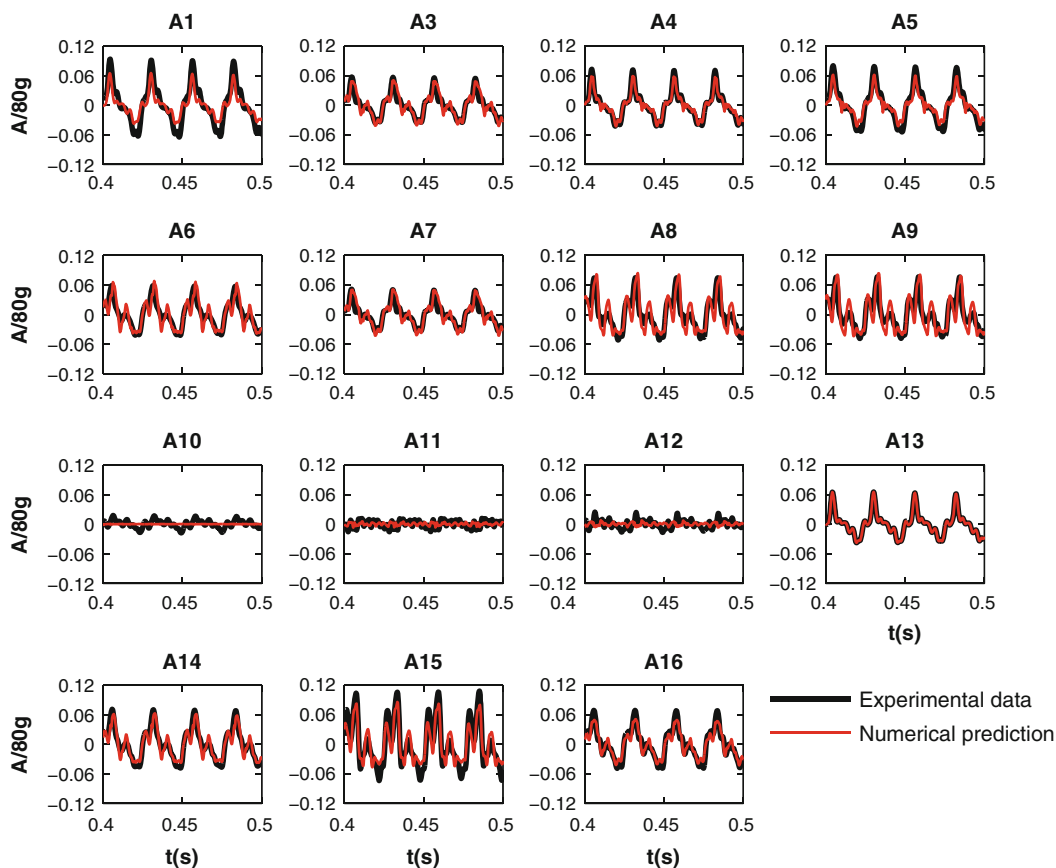


Fig. 10 Windows of acceleration time histories for test T3-EQ2; experimental records versus numerical analysis predictions

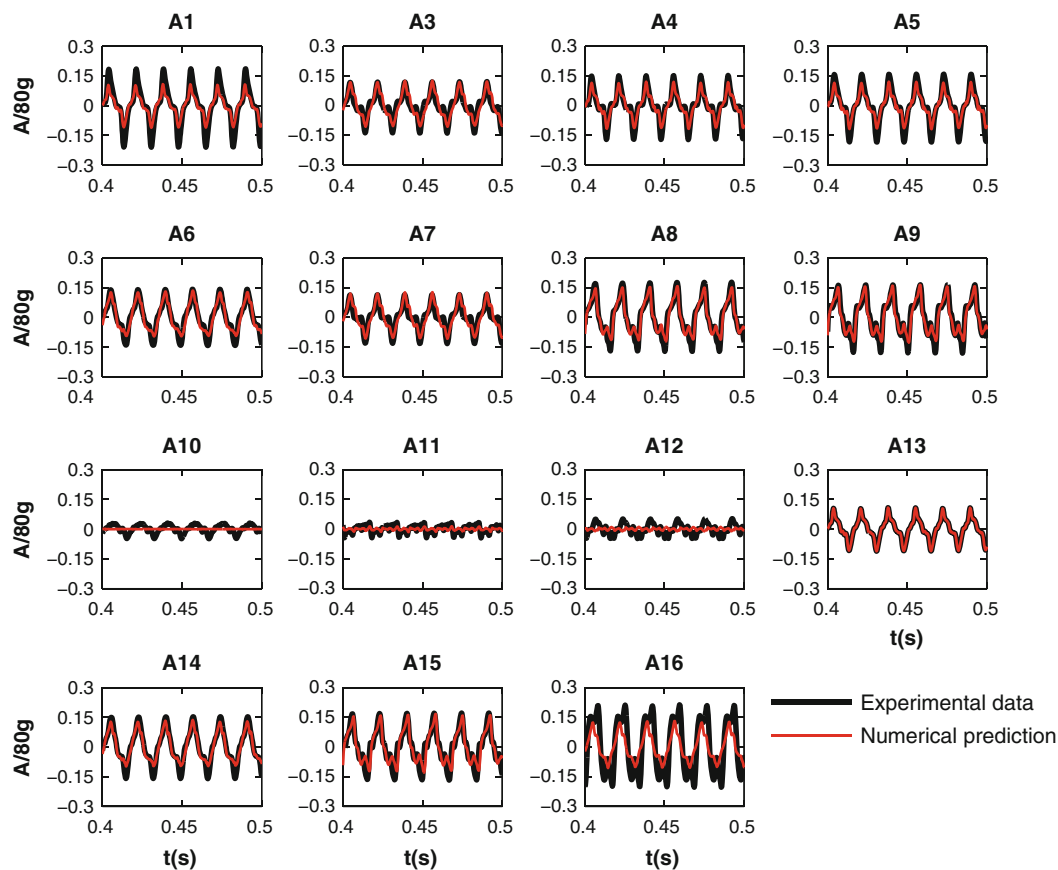


Fig. 11 Windows of acceleration time histories for test T3-EQ4; experimental records versus numerical analysis predictions

accelerometers arrays, according to the simplified procedure proposed by Zeghal and Elgamal [27] (Figs. 17, 18). More specifically, from the recorded acceleration time histories, the displacement time histories are computed through double integration. The mobilized shear strain between two accelerometers, along the same vertical array, may be evaluated as follows:

$$\gamma = \frac{(u_2 - u_1)}{(z_2 - z_1)} \quad (13)$$

where u_1 and u_2 are the displacement time histories, and z_1 and z_2 the depths of the examined accelerometers.

The numerically predicted strains were found to be generally lower with respect to the strains estimated from the experimental data. The deviations can be attributed to several reasons and to some extent to the differences between the assumed and the actual soil mechanical properties, in particular around the tunnel. It should be also noted that for the computation of the strains from the experimental data, the soil settlements (caused by the increase in gravitational load during swing up and the subsequent shaking) were not taken into account, as we did not know their actual distribution within the deposits. These settlements may cause changes to the distances

between the receivers, affecting significantly the estimated strains. Despite the differences, considering the complexity of the problem in overall, the order of magnitude is correctly estimated.

4.5 Dynamic internal forces

Figure 19 presents representative recorded dynamic bending moment time histories of the tunnel lining (NE and NW sections), while in Fig. 20, dynamic axial force time histories recorded at SE and NE sections are presented. The recorded time histories are given for both test cases and compared with the numerical predictions.

From both the axial force and the bending moment records, three distinctive stages may be identified for the tunnel lining response, namely a transient stage followed by a steady-state stage and finally a post-earthquake residual stage. This behavior that is actually expected for very flexible structures has also been verified by similar dynamic centrifuge tests on square tunnel models embedded in dry sand [4, 23, 24]. Generally, it can be attributed to the soil densification and/or soil yielding during shaking that cause stress redistributions in the soil around the tunnel. Small sliding effects at the soil–tunnel interface can

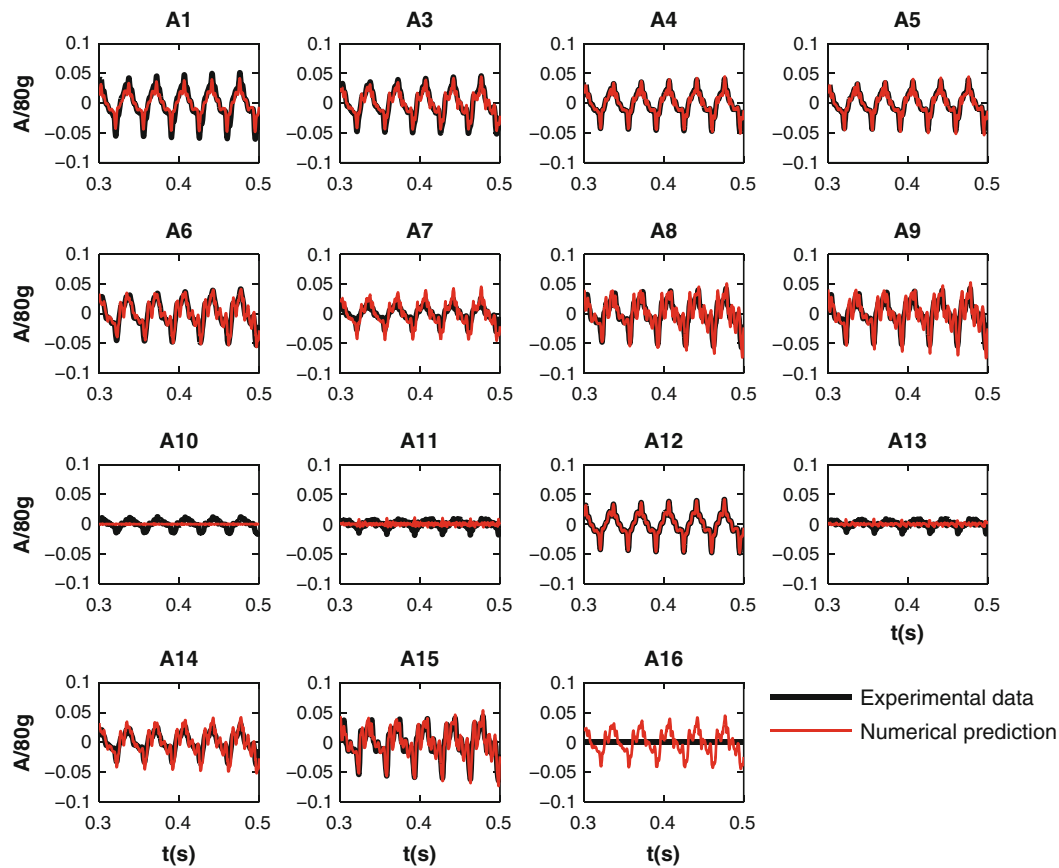


Fig. 12 Windows of acceleration time histories for test T4-EQ1; experimental records versus numerical analysis predictions (A16 did not record during this earthquake)

also affect this behavior (e.g., for the axial forces). It is noted that the internal forces residuals are significantly amplified by the high flexibility of the tunnel lining. Actually, the selected lining thickness is unrealistic in practice, as static loads would result in a much thicker choice. However, the selection was made so as to be possible to achieve clear measurements of the lining strains.

Although the numerical models did not manage to capture the exact evolution of the recorded dynamic internal forces, similar phenomena (aforementioned stages, residual values, etc.) were observed, while the recorded and the computed data were in the same order of magnitude. The differences between the computed and the recorded data can be mainly attributed to the differences between the assumed mechanical properties of the sand, the tunnel, and the interface with the actual values and response during the tests. For example, the preclusion of the tube plastic behavior from the numerical analyses can cause differences between the computed and the recorded tunnel response. Actually, plastic deformations of the tube (tunnel) may cause the inversion of the polarity of the lining internal forces. Finally, uncertainties related to the calibration procedure of the strain gauges could also affect to some

extend the differences between the experimental and the computed values.

Figures 21, 22, 23, and 24 summarize the computed dynamic increments of the internal forces, for both tests, compared to the experimental data. These increments are computed as the maximum values of the semi-amplitude of cycles in the time histories, during the steady-state stage. The results are also compared with the predictions of closed-form solutions, usually applied at the preliminary stages of tunnels design [18, 26]. The solutions, summarized in “Appendix,” refer to computation of the axial forces and the bending moments of the tunnel lining under S-wave propagation, assuming the full-slip zero friction conditions for the interface. For the implementation of the solutions herein, the shear strain γ_{\max} was estimated using the results of the 1D equivalent linear soil response analyses presented before (calibration procedure of the soil constitutive model).

Generally, the numerical predictions are in the same order of magnitude with the closed-form solutions and the experimental data, and for some excitations, the numerical results are very close to the experimental data. As mentioned, the reported differences can be attributed to the

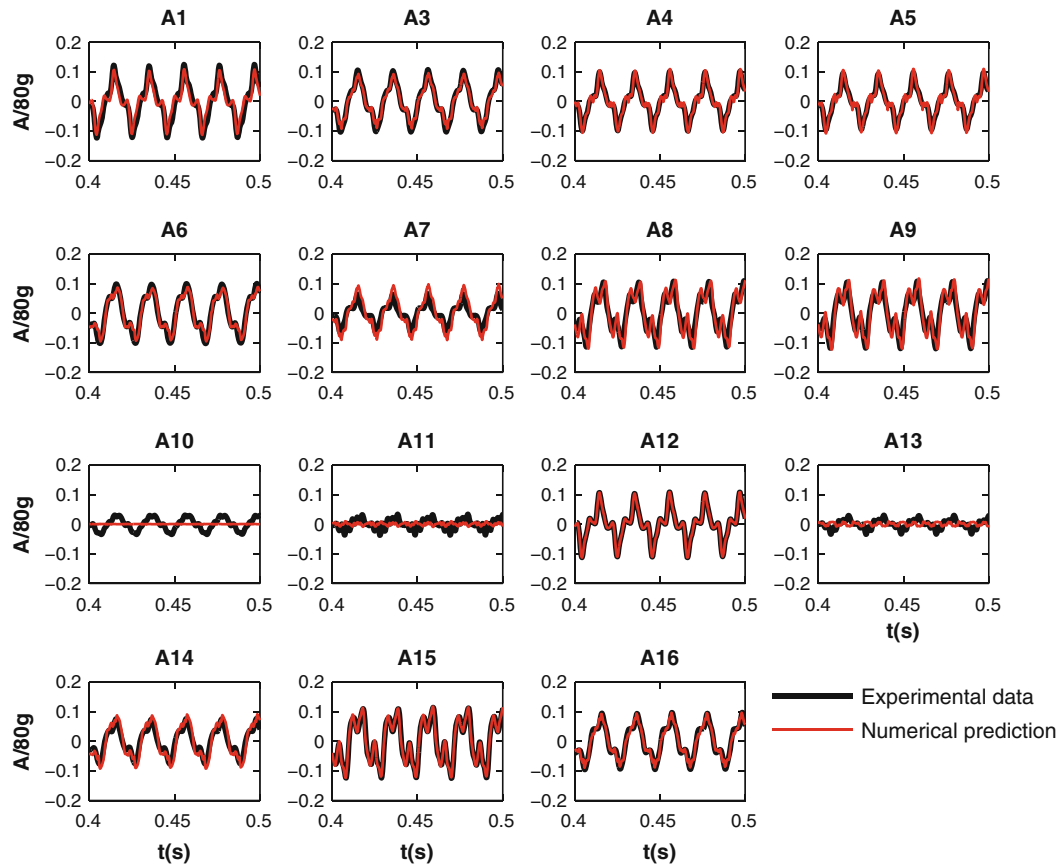


Fig. 13 Windows of acceleration time histories for test T4-EQ3; experimental records versus numerical analysis predictions

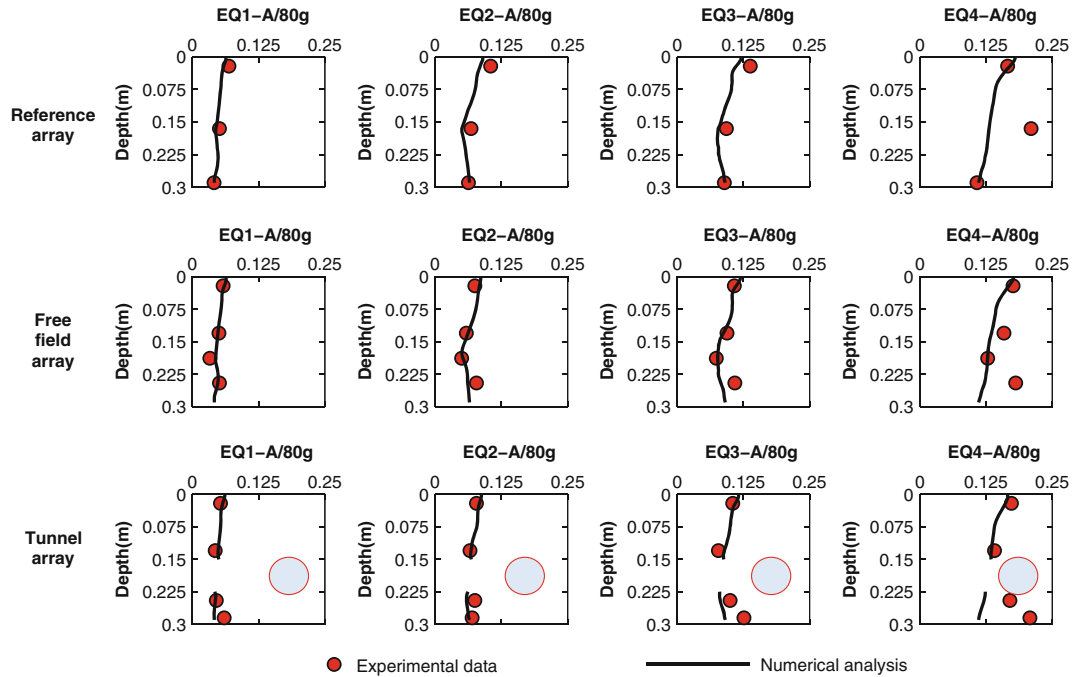


Fig. 14 Computed and recorded maximum horizontal acceleration along vertical accelerometers arrays for T3 test

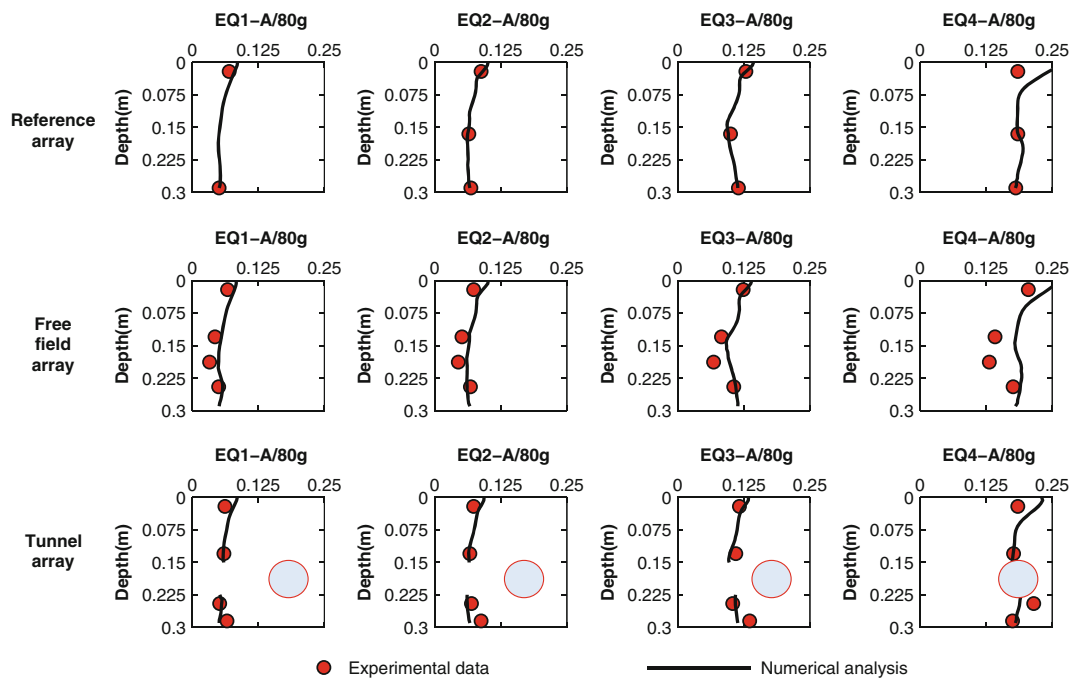


Fig. 15 Computed and recorded maximum horizontal acceleration along vertical accelerometers arrays for T4 test

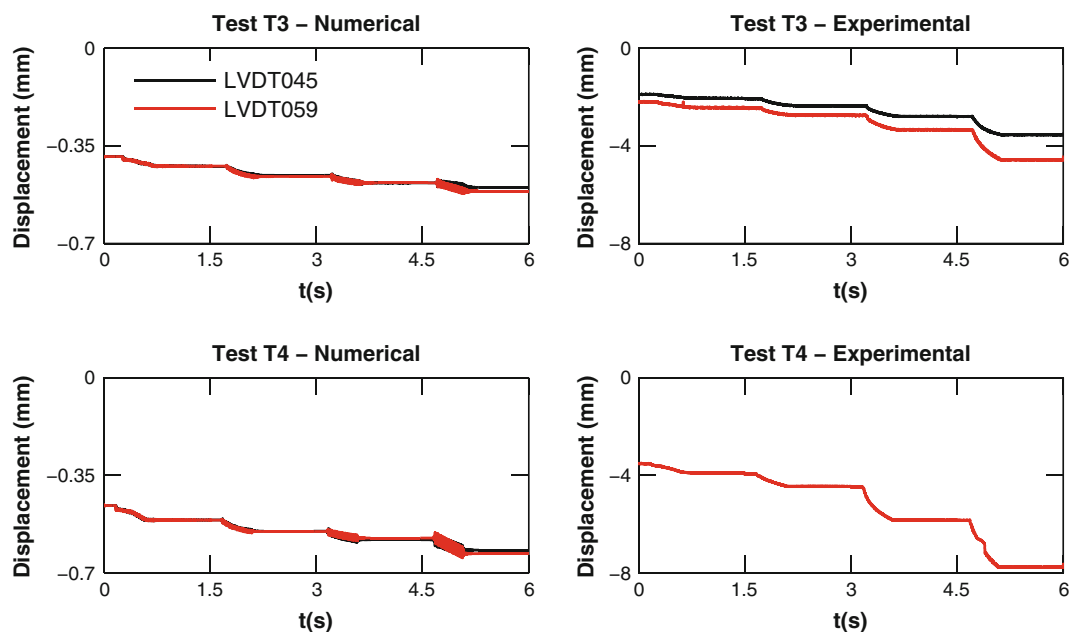


Fig. 16 Computed and recorded soil surface settlements for both the tests

differences between the assumed and the actual mechanical properties of the soil, the tunnel, and the interface. The accurate estimation of these parameters is of prior importance for the tunnel response. However, this estimation is very difficult for this type of complex experiments.

The closed-form solutions generally under-predict the tunnel axial force increments with respect to the experimental data and the numerical results, while the opposite

is observed for the bending moment increments. It is noted that the solutions are based on simplified assumptions (e.g., elastic homogeneous soil, infinite bonding of the soil–tunnel interface in the normal direction, etc.) that are not probably entirely valid for the cases studied herein. This could explain to some extent the observed differences between the numerical predictions and the solutions results.

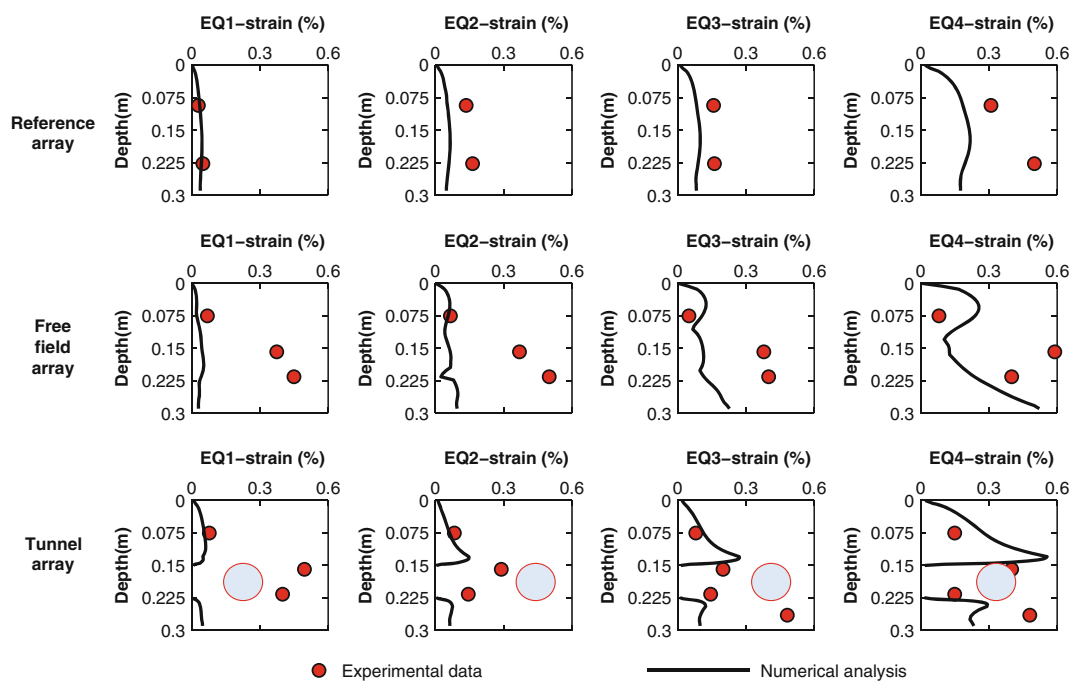


Fig. 17 Soil shear strains along vertical accelerometers arrays for test T3; numerical analysis versus experimental data (shear strains derived from acceleration time histories)

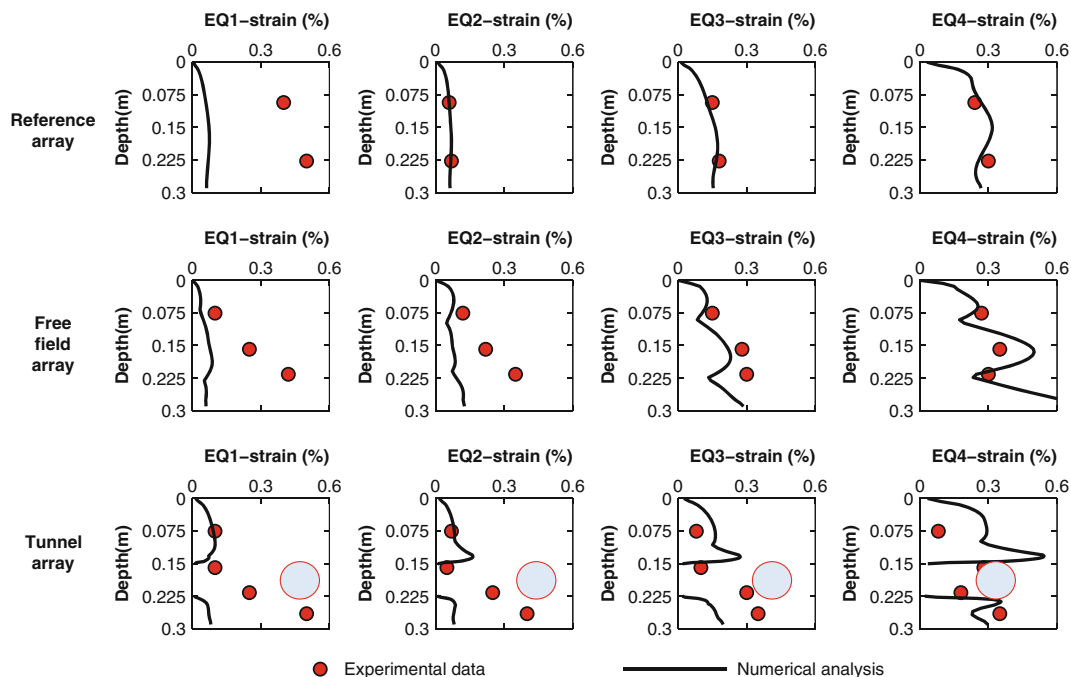


Fig. 18 Soil shear strains along vertical accelerometers arrays for test T4; numerical analysis versus experimental data (shear strains derived from acceleration time histories)

4.6 Effect of the tangential friction on the tunnel response

Figures 25 and 26 present the dynamic increments of the tunnel internal forces (maximum values of the semi-

amplitude of cycles in the time histories) computed for EQ1 and EQ4 of T3 model, assuming different friction coefficients for the soil–tunnel interface. Results, assuming no-slip perfect bonding conditions for the interface, are also presented and compared. As shown, the effect of the

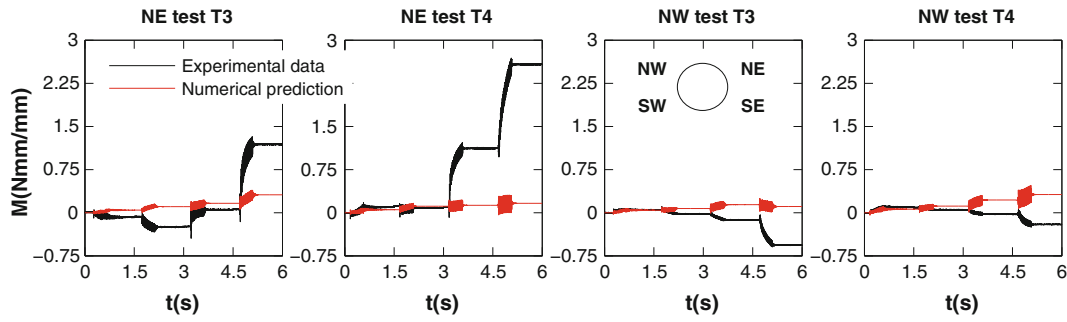


Fig. 19 Bending moment time histories at NE and NW locations of the tunnel lining; experimental data versus numerical results

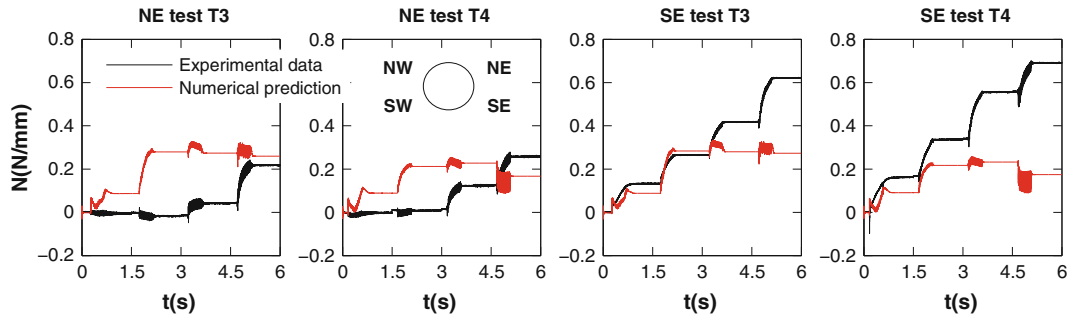


Fig. 20 Axial force time histories at NE and SE locations of the tunnel lining; experimental data versus numerical results

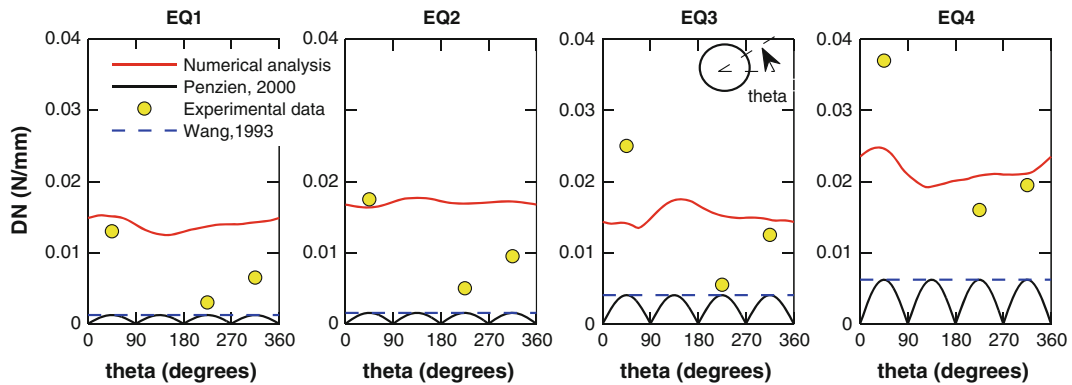


Fig. 21 Axial force dynamic increments for T3 test; numerical predictions versus experimental data and closed-form solutions results

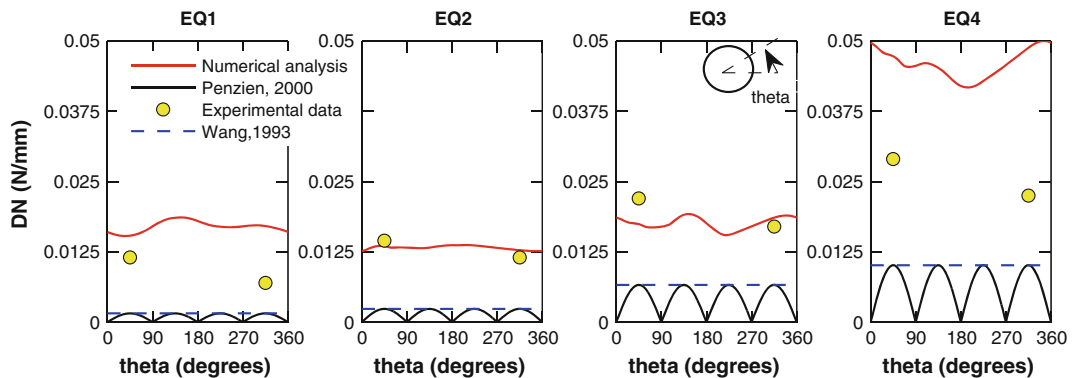


Fig. 22 Axial force dynamic increments for T4 test; numerical predictions versus experimental data and closed-form solutions results

mobilized along the interface friction, on the lining axial forces, is very important, while for the bending moments, this effect seems to be less important. Similar observations may be found in the literature [9, 13, 21]. The experimental results seem to better correlate with the full-slip conditions assumption.

The soil–tunnel interface behavior is actually one crucial parameter that controls the soil–tunnel system behavior. This behavior can affect the soil nonlinear response at the vicinity of the tunnel. For example, a more “rigid” connection of the tunnel with the soil (e.g., larger coefficient of friction) can affect the soil stiffness degradation

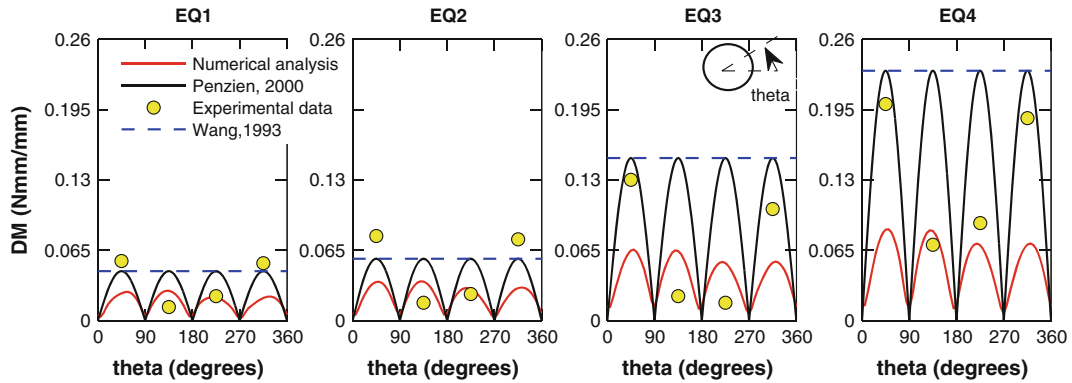


Fig. 23 Bending moment dynamic increments for T3 test; numerical predictions versus experimental data and closed-form solutions results

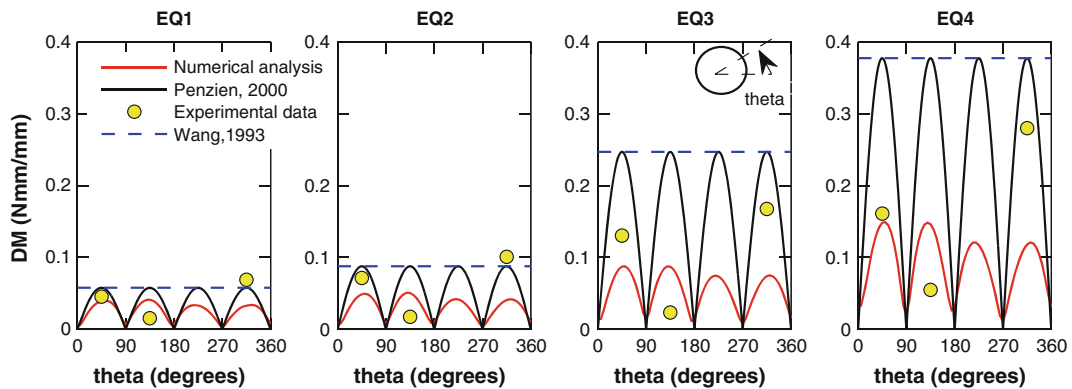


Fig. 24 Bending moment dynamic increments for T4 test; numerical predictions versus experimental data and closed-form solutions results

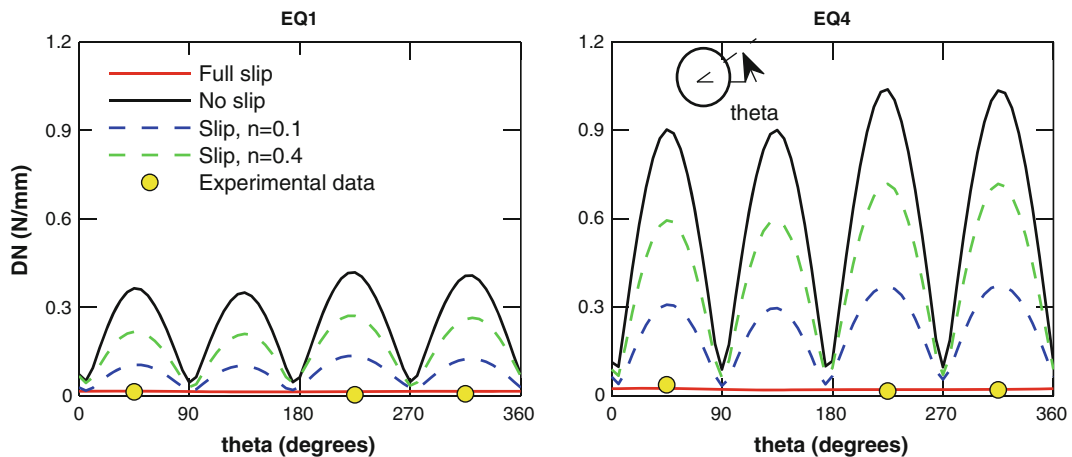


Fig. 25 Axial force dynamic increments computed for different values of tangential friction on the interface

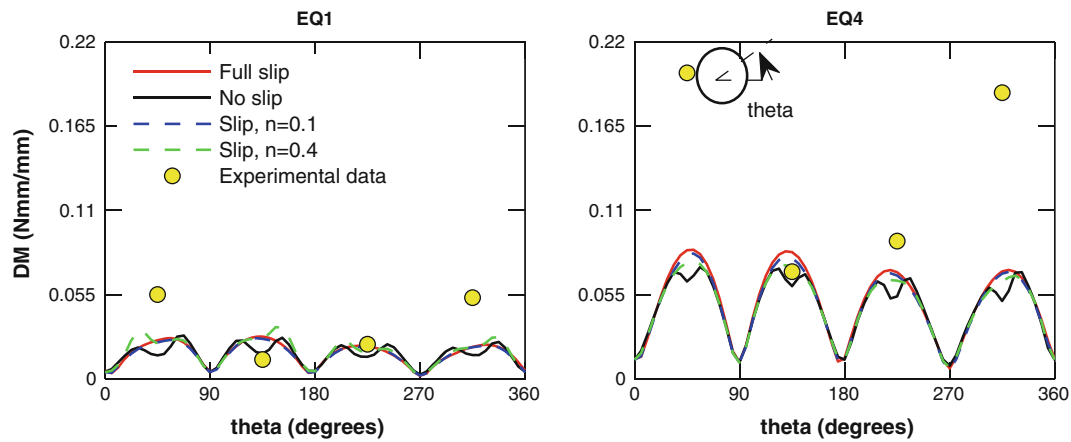


Fig. 26 Bending moment dynamic increments computed for different values of tangential friction on the interface

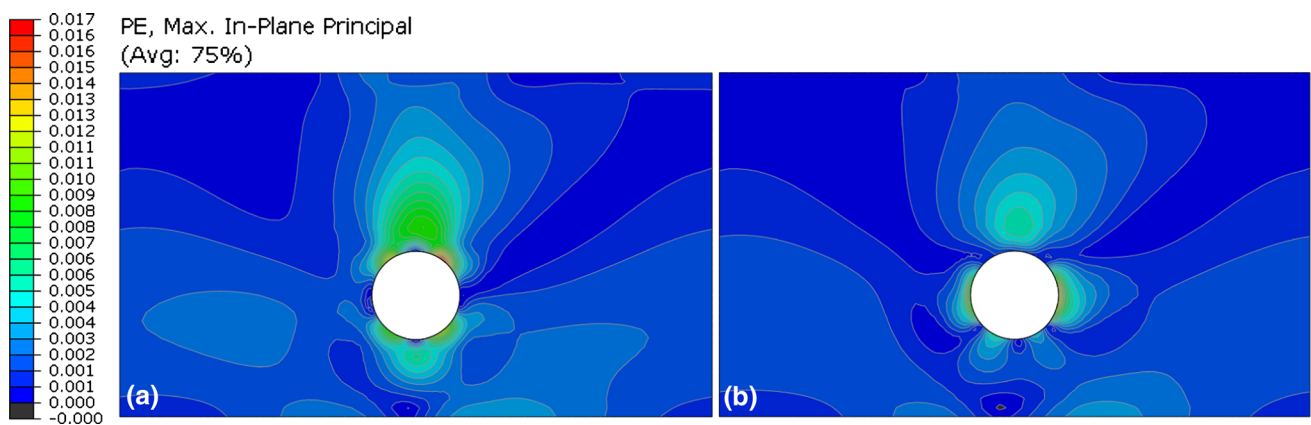


Fig. 27 Plastic strains at the end of EQ4 for T3 model; a full-slip conditions, b no-slip conditions

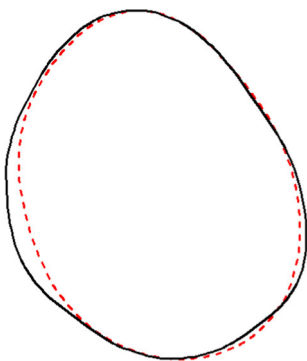


Fig. 28 Tunnel lining deformed shape for time step 4.75 s (EQ4-T3 test); solid line no-slip conditions, dashed line full-slip conditions

due to yielding near the tunnel, resulting in different stress redistributions in the soil around the tunnel. Figure 27 presents the soil plastic strains of the soil model, computed at the end of EQ4 for the test T3, for two assumptions regarding the interface, namely the full-slip (Fig. 27a) and the no-slip (Fig. 27b) conditions. Differences in the

distributions can be observed. These discrepancies are actually causing minor differences on the tunnel deformation modes (Fig. 28).

5 Conclusions

The paper summarizes the numerical simulation of RRTT performed in Aristotle University of Thessaloniki. Representative comparisons of the numerical predictions with the experimental data were presented and discussed, in terms of acceleration, soil settlements, soil shear strains, and dynamic internal forces of the tunnel lining. Soil nonlinear behavior was modeled with a simplified kinematic hardening model. The model was calibrated using available laboratory test results. The soil–tunnel interface was also simulated, and the effect of the interface friction on the tunnel response was studied. The main conclusions drawn may be summarized in the following:

- Although the implemented model constitutes an approximation of the actual sand behavior, it was

found capable to reproduce several aspects of the recorded response, with reasonable engineering accuracy.

- The recorded amplification of the horizontal acceleration is efficiently modeled in the numerical analyses.
- Residual values were recorded and computed after each shake for the lining internal forces (axial forces and bending moments), as a result of cumulative strains during the shaking. These residual internal forces were strongly affected and amplified by the flexibility of the tunnel.
- The numerical models used herein reproduced the general trends observed from the recorded dynamic internal forces (residual values, dynamic increments). The differences between the computed and the recorded values are attributed to several reasons, namely the differences between the estimated soil, tunnel, and soil–tunnel interface mechanical properties, compared to the real test values that are difficultly known. Errors related to the quality of the records (e.g., poor calibration of the instruments) could also cause important differences.
- The mobilized friction at the interface is significantly affecting the lining axial forces, while the effect is less pronounce or negligible for the bending moments.
- Generally, we conclude that considering all kind of uncertainties involved, numerical models may reproduce quite satisfactorily the recorded response in the centrifuge.

Acknowledgments The authors acknowledge the RRTT organizers for their support and cooperation during the program. The first author would like to acknowledge Assistant Professor Ioannis Anastasopoulos and Dr. Fani Gelagoti for the fruitful discussions he had with, for the implementation of the kinematic hardening model.

Appendix

According to Wang [26] and assuming the full-slip conditions, the following formulations are proposed for the computation of the maximum axial force (N_{\max}) and bending moment (M_{\max}) of the lining:

$$M_{\max} = \pm \frac{1}{6} K_1 \frac{E_m}{(1 + \nu_m)} R^2 \gamma_{\max} \quad (14)$$

$$N_{\max} = \pm \frac{1}{6} K_1 \frac{E_m}{(1 + \nu_m)} R \gamma_{\max} \quad (15)$$

where

$$K_1 = \frac{12(1 - \nu_m)}{2F + 5 - 6\nu_m} \quad (16)$$

and

$$F = \frac{E_m(1 - \nu_1^2)R^3}{6E_1I_1(1 + \nu_m)} \quad (17)$$

the flexibility ratio. E_m is the soil elastic modulus, ν_m is the soil Poisson ratio, E_1 is the lining elastic modulus, ν_1 is the lining Poisson ratio, I_1 is the moment of inertia of the tunnel lining (per unit width), R is the tunnel radius, and γ_{\max} the maximum shear strain at tunnel depth.

According to Penzien [18], the lining internal forces can be computed, assuming the full-slip conditions, using the following expressions:

$$N(\theta) = -\frac{12E_1I_1\Delta d_{\text{stru}}^n}{D^3(1 - \nu_1^2)} \cos 2\left(\theta + \frac{\pi}{4}\right) \quad (18)$$

$$M(\theta) = -\frac{6E_1I_1\Delta d_{\text{stru}}^n}{D^2(1 - \nu_1^2)} \cos 2\left(\theta + \frac{\pi}{4}\right) \quad (19)$$

where $N(\theta)$ and $M(\theta)$ are the axial force and the bending moment, respectively, and D is the tunnel diameter and:

$$\pm \Delta d_{\text{stru}}^n = \pm R^n \Delta d_{\text{ff}} \quad (20)$$

$$R^n = \frac{\Delta d_{\text{stru}}^n}{\Delta d_{\text{ff}}} = \pm \frac{4(1 - \nu_m)}{(1 + a^n)} \quad (21)$$

$$a^n = \frac{12(5 - 6\nu_m)E_1I_1}{D^3G_m(1 - \nu_1^2)} \quad (22)$$

with G_m being the soil shear modulus and Δd_{ff} the free-field ovaling distortion correlated with the shear strain γ_{\max} .

References

1. ABAQUS (2010) Analysis user's manual-version 6.10. Dassault Systèmes, SIMULIA Inc, USA
2. Anastasopoulos I, Gelagoti F, Kourkoulis R, Gazetas G (2011) Simplified constitutive model for simulation of cyclic response of shallow foundations: validation against laboratory tests. *J Geotech Geoenviron Eng* 137(12):1154–1168
3. Bardet JB, Ichii K, Lin CH (2000) EERA: a computer program for equivalent-linear earthquake site response analyses of layered soil deposits. University of Southern California, Department of Civil Engineering, California, p 40
4. Cilingir U, Madabhushi SPG (2011) A model study on the effects of input motion on the seismic behavior of tunnels. *J Soil Dyn Earthq Eng* 31:452–462
5. Darendeli M (2001) Development of a new family of normalized modulus reduction and material damping curves. Ph.D. Dissertation, University of Texas at Austin
6. Federal Highway Administration (2009) Technical manual for design and construction of road tunnels—civil elements. U.S. Department of transportation. Federal Highway Administration. Publication No. FHWA-NHI-10-034, p 702
7. Hardin BO, Drnevich VP (1972) Shear modulus and damping in soils: design equations and curves. *J Soil Mech Found Div* 98(SM7):667–692

8. Hashash YMA, Hook JJ, Schmidt B, Yao JI-C (2001) Seismic design and analysis of underground structures. *Tunn Undergr Space Technol* 16(2):247–293
9. Hashash YMA, Park D, Yao JIC (2005) Ovaling deformations of circular tunnels under seismic loading, an update on seismic design and analysis of underground structures. *Tunn Undergr Space Technol* 20:435–441
10. ISO 23469 (2005) Bases for design of structures—seismic actions for designing geotechnical works. International Standard ISO TC 98/SC3/WG10
11. Kawashima K (2000) Seismic design of underground structures in soft ground: a review. In: Kusakabe O, Fujita K, Miyazaki Y (eds) *Geotechnical aspects of underground construction in soft ground*. Balkema, Rotterdam
12. Kontoe S, Zdravkovic L, Potts D, Mentiki C (2008) Case study on seismic tunnel response. *Can Geotech J* 45:1743–1764
13. Kouretzis G, Sloan S, Carter J (2013) Effect of interface friction on tunnel liner internal forces due to seismic S- and P-wave propagation. *J Soil Dyn Earthq Eng* 46:41–51
14. Lanzano G, Bilotta E, Russo G, Silvestri F, Madabhushi SPG (2010) Dynamic centrifuge tests on shallow tunnel models in dry sand. In: *Proceedings of the VII international conference on physical modelling in geotechnics (ICPMG 2010)*. Taylor & Francis, Zurich, pp 561–567
15. Lanzano G, Bilotta E, Russo G, Silvestri F, Madabhushi SPG (2012) Centrifuge modelling of seismic loading on tunnels in sand. *Geotech Test J* 35(6):854–869. doi:[10.1520/GTJ104348](https://doi.org/10.1520/GTJ104348)
16. Madabhushi SPG, Schofield AN, Lesley S (1998) A new stored angular momentum (SAM) based actuator. In: Kimura T, Kusakabe O, Takemura J (eds) *Centrifuge 98*. AA Balkema publishers, Tokyo, Japan, pp 111–116
17. Owen GN, Scholl RE (1981) Earthquake engineering of large underground structures. Report No. FHWA/RD-80/195, Federal Highway Administration and National Science Foundation, 279 p
18. Penzien J (2000) Seismically induced racking of tunnel linings. *Earthq Eng Struct Dyn* 29:683–691
19. Pitilakis K, Tsinidis G (2012) Performance and seismic design of underground structures. In: *II international conference on performance based design in earthquake geotechnical engineering (State of the art lecture)*, May 2012, Taormina, Italy
20. Schofield AN (1981) Cambridge geotechnical centrifuge operations. *Geotechnique* 30(3):227–268
21. Sederat H, Kozak A, Hashash YMA, Shamsabadi A, Krimotat A (2009) Contact interface in seismic analysis of circular tunnels. *Tunn Undergr Space Technol* 24(4):482–490
22. Tsinidis G, Pitilakis K (2012) Seismic performance of circular tunnels: centrifuge testing versus numerical analysis. In: *II international conference on performance based design in earthquake geotechnical engineering*, May 2012, Taormina, Italy
23. Tsinidis G, Pitilakis K, Heron C, Madabhushi SPG (2013) Experimental and numerical investigation of the seismic behavior of rectangular tunnels in soft soils. In: *Computational methods in structural dynamics and earthquake engineering conference (COMPEDYN 2013)*, June 2013, Kos, Greece
24. Tsinidis G, Heron C, Pitilakis K, Madabhushi G (2013) Physical modeling for the evaluation of the seismic behavior of square tunnels. In: Ilki A, Fardis MN (eds) *Seismic evaluation and rehabilitation of structures*. *Geotech Geolog Earthq Eng*, vol 26, pp 389–406. doi:[10.1007/978-3-319-00458-7_22](https://doi.org/10.1007/978-3-319-00458-7_22)
25. Visone C, Santucci de Magistris F (2009) Mechanical behavior of the Leighton Buzzard Sand 100/170 under monotonic, cyclic and dynamic loading conditions. In: *Proceedings of the XIII conference on L' Ingegneria Sismica in Italia*, ANIDIS, Bologna, Italy
26. Wang JN (1993) *Seismic design of tunnels—a simple state-of-the-art design approach*. Parson Brinckerhoff, New York
27. Zeghal M, Elgamal AW (1994) Analysis of site liquefaction using earthquake records. *J Geotech Eng ASCE* 120(6):996–1017